Northumbria Research Link

Citation: Li, Dongsheng, Liu, Weiting, Zhu, Boyi, Qu, Mengjiao, Zhang, Qian, Fu, Yong Qing and Xie, Jin (2022) Machine Learning-Assisted Multifunctional Environmental Sensing Based on a Piezoelectric Cantilever. ACS Sensors, 7 (9). pp. 2767-2777. ISSN 2379-3694

Published by: American Chemical Society

URL: https://doi.org/10.1021/acssensors.2c01423 <https://doi.org/10.1021/acssensors.2c01423>

This version was downloaded from Northumbria Research Link: https://nrl.northumbria.ac.uk/id/eprint/50060/

Northumbria University has developed Northumbria Research Link (NRL) to enable users to access the University's research output. Copyright © and moral rights for items on NRL are retained by the individual author(s) and/or other copyright owners. Single copies of full items can be reproduced, displayed or performed, and given to third parties in any format or medium for personal research or study, educational, or not-for-profit purposes without prior permission or charge, provided the authors, title and full bibliographic details are given, as well as a hyperlink and/or URL to the original metadata page. The content must not be changed in any way. Full items must not be sold commercially in any format or medium without formal permission of the copyright holder. The full policy is available online: http://nrl.northumbria.ac.uk/policies.html

This document may differ from the final, published version of the research and has been made available online in accordance with publisher policies. To read and/or cite from the published version of the research, please visit the publisher's website (a subscription may be required.)

Northumbria University NEWCASTLE

CUSTOMER SERVICE EXCELLENCE CSE UniversityLibrary

Machine Learning-Assisted Multifunctional Environmental Sensing Based on Piezoelectric Cantilever

Dongsheng Li[1], Weiting Liu[1, *], Boyi Zhu[1], Mengjiao Qu[1], Qian Zhang[1], YongQing Fu[2], and Jin Xie[1, *]

[1] State Key Laboratory of Fluid Power and Mechatronic Systems, Zhejiang University, Hangzhou, Zhejiang, 310027, P. R. China

[2] Faculty of Engineering and Environment, University of Northumbria, Newcastle upon Tyne NE1 8ST, UK

*Corresponding author. E-mail: liuwt@zju.edu.cn; xiejin@zju.edu.cn

KEYWORDS: AlN piezoelectric cantilever, Environmental sensor, Human-machine interaction, Machine learning, MoS_2, Multifunctional sensor

ABSTRACT: Multifunctional environmental sensing is crucial for various applications in agriculture, pollution monitoring, and disease diagnosis. However, most of these sensing systems consist of multiple sensors, leading to significantly increased dimensions, energy consumption, and structural complexity. They also often suffer from signal interferences among multiple sensing elements. Herein, we report a multifunctional environmental sensor based on one single sensing element. A MoS_2 film was deposited on the surface of a piezoelectric micro-cantilever (300×1000 μm^2) and used as both a sensing layer and top electrode to make full use of the changes in multiple properties of MoS_2 after its exposure to various environments. The proposed sensor has been demonstrated for humidity detection, and achieved a high resolution (0.3% RH), low hysteresis (5.6%), and fast response (1 s) and recovery (2.8 s). Based on the analysis of the magnitude spectra for transmission using machine-learning algorithms, the sensor accurately quantifies temperature and CO_2 concentrations in the interference of humidity with the accuracies of 91.9% and 92.1%, respectively. Furthermore, the sensor has been successfully demonstrated in real-time detections of humidity and temperature or CO_2 concentrations for various applications, revealing its great potentials in human-machine interactions and health monitoring of plants and human beings.

Environmental sensors, e.g., humidity sensor, temperature sensor, gas sensor, etc., have wide-range applications in many fields such as pollution monitoring, internet of things (IoT), and disease diagnosis.[1-3] Recently monitoring plant ecosystem and human health based on environmental sensors has attracted extensive research attention because of its simplicity, low cost, and non-invasive operation capabilities.[4-6] However, most conventional environmental sensors can only detect one single parameter, which is insufficient for the full assessment of environment or health conditions.[7] Therefore, there is a great demand to develop multifunctional environmental sensors that not only have excellent performances, e.g., high sensitivity, but also simultaneously monitor the multiple signals.

There have been many studies to develop multifunctional sensors for detecting different stimuli simultaneously, and they are mainly divided into two directions.[8] The first direction is to develop multimodal sensors, which can respond to multiple stimuli,[9] enabling the detection of multiple parameters using a single sensor. For example, Wang *et al* reported a multimodal sensor to detect multiple stimuli including gases, light, strain, pressure, temperature, and humidity.[10] However, the output signals of these sensors are often a superposition of responses to multiple stimuli, and decoupling these responses based on a single sensor is rather difficult, which limits their wide-range applications. Another direction is to apply a multi-sensor system, where various sensing elements, which do not need to share the same sensing principles, are physically integrated into one sensing system and each sensor is assigned to detect a defined stimulus.[11, 12] For example, Xu *et al* proposed an integrated system composed of tilt, strain, and humidity sensors for tracking human-body conditions.[13] However, this method often leads to large dimensions of the sensor, complex structures, and complicated fabrication processes. The integration of multiple sensors into one platform is often linked with significant increases in energy consumption and decreases in stability and reliability, while the sensing platform also suffers from signal interferences among the multiple sensing elements.[14] Recently, some multifunctional sensors based on a single sensing element and machine learning have been developed.[15-17] However, how to detect multiple environmental parameters simultaneously using a single element is still a challenge.

The development of micro electro-mechanical systems (MEMS) technology promotes the miniaturization of environmental sensors, and many environmental sensors have been developed based on different principles such as optical sensors, chemiresistors, electrochemical sensors, and field effect transistors (FET).[18-20] Among them, piezoelectric cantilever is one of the most promising environmental sensing platforms because of its advantages of small size, large sensing range, compatibility with CMOS processes, and easy interfacing with digital circuits.[21, 22] The piezoelectric cantilever-based environmental sensors usually consist of a cantilever with a sensing layer, whose properties, such as mass, viscoelasticity, and electrical conductivity, will be changed after its exposure to various environments.[23-25] However, the metallic top electrode of the conventional piezoelectric cantilever, which is normally covered by the sensing layer, as shown in **Figure S1**, usually has excellent electrical conductivity, which eliminates the effects of the conductivity changes of the sensing film on the output signal of the sensor. Currently most environmental sensors based on the piezoelectric cantilevers only detect their resonant frequency shifts after exposure to various environments, which are mainly due to mass changes of the sensing film.[26] Whereas changes in other properties (e.g., viscoelasticity and conductivity) of the sensing film for the cantilever-based sensor have rarely been considered, leading to a serious waste of much crucial information.[27]

Two-dimensional materials such as graphene have been widely studied for environmental sensing applications because of their excellent electrical and mechanical properties, high surface-to-volume ratios, versatile surface chemistry, and capability of room-temperature detection.[28, 29] For example, the resistance of graphene will be changed after exposure to volatile organic compounds (VOCs) because of the

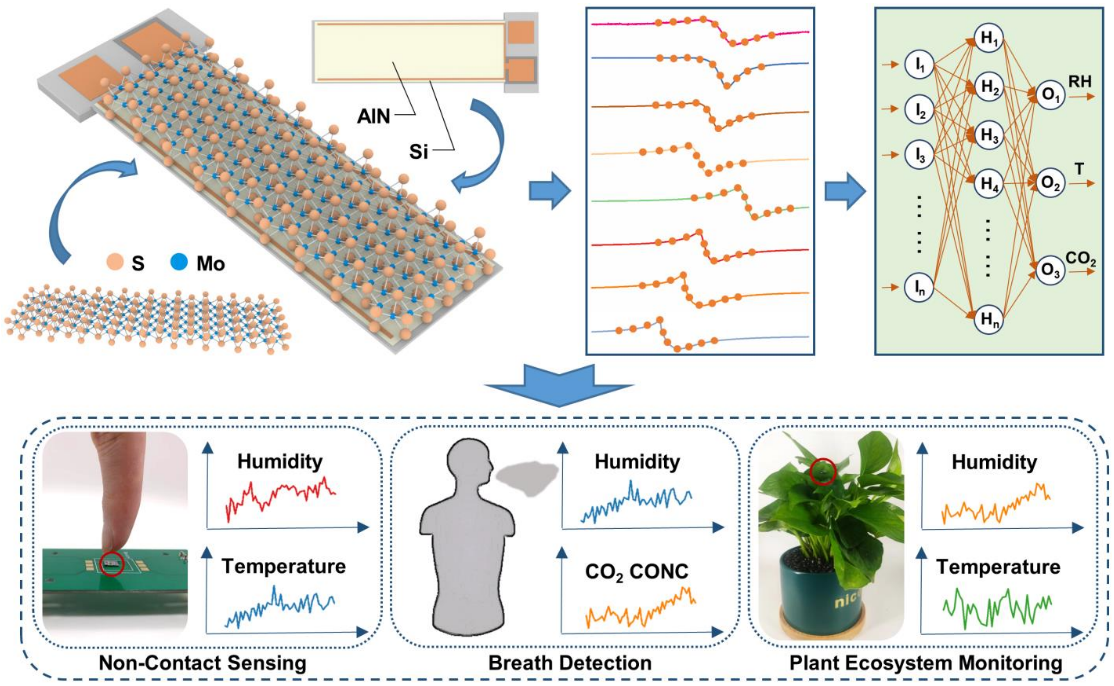

Figure 1. Schematic diagrams of the proposed multifunctional environmental sensor.

doping effect of VOC molecules.[29] However, graphene has often shown weak adsorption capability to gas molecules, thus a low sensitivity for gas sensing.[30] Compared with graphene, molybdenum disulfide (MoS_2) with excellent electrical properties exhibits larger responses to gas molecules, and the MoS_2-based environmental sensors are often reported to have fast response and recovery.[31, 32] Therefore, MoS_2 is a suitable sensing material for environmental sensing applications.

In this work, we propose a multifunctional environmental sensor based on a single piezoelectric cantilever without conventional top electrode, as schematically shown in **Figure 1**. The MoS_2 film was deposited on the surface of the cantilever as both the top electrode and sensing layer to make full use of the changes in multiple properties of MoS_2 after exposure to various environments. The frequency responses of the sensor to various humidity levels were tested and the performances of the sensor (e.g., sensitivity and resolution) were investigated systematically. Based on the analysis of the magnitude spectra for transmission using machine learning algorithms, the sensor was demonstrated to detect temperature and CO_2 concentration with the interference of humidity. The sensor was further applied in real-time detections of humidity and temperature or CO_2 concentration for non-contact sensation and monitoring human breath and plant ecosystem, as shown in Figure 1.

RESULTS AND DISSCUSSION

Characterizations of the Fabricated Sensor. The proposed environmental sensor consists of a piezoelectric cantilever and MoS_2 film, as shown in Figure 1. **Figures 2a**, **S2a**, and **S2b** show the optical images of the piezoelectric cantilever. In order to make full use of the changes in multiple properties of MoS_2 after its exposure to various environments, the cantilever without conventional top electrode was designed as shown in **Figure S3**. The area of the cantilever was 300×1000 μm^2. An aluminum nitride (AlN) layer with a thickness of 0.5 μm was coated onto the silicon (Si) layer as the piezoelectric layer. The thermal oxide layer, Si layer, and highly-doped surface of the Si layer were applied as an insulating layer, structural layer, and bottom electrode, respectively. **Figure 2b** shows a scanning electron microscope (SEM) image of the proposed sensor after MOS_2 deposition. A MoS_2 layer is formed on the surface of the cantilever. **Figure 2c** shows the surface morphology of the MoS_2 film, revealing a uniform MoS_2 film. **Figure 2d** shows the energy dispersive X-ray spectroscope (EDS) analysis for the elements of Mo and S, indicating their even distribution across the entire film.

Figure 2e shows Raman spectroscopy of the MoS_2 film. There are two representative Raman absorption peaks E_{2g}^{1} = 380.2 cm^{-1} and A_{1g} = 405.8 cm^{-1}, which can be assigned to the in-plane vibration and out-of-plane phonon coupling mode of MoS_2, respectively, indicating the few-layer property of the MoS_2 film.[33, 34] **Figure 2f** shows the Mo 3d spectrum from the X-ray photoelectron spectroscopy (XPS) analysis of the MoS_2 film. The Mo 3d spectrum can be fitted with two doublets (Mo $3d_{3/2}$, Mo $3d_{5/2}$) with an area ratio of 2:3 and the doublet separation was 3.15 eV. The four peaks at 235.6 eV, 232.5 eV, 231.8 eV, and 228.7 eV, are associated with the Mo $3d_{3/2}$ of Mo^{6+}, Mo $3d_{5/2}$ of Mo^{6+}, Mo $3d_{3/2}$ of Mo^{4+}, and Mo $3d_{5/2}$ of Mo^{4+}, respectively.[35] The Mo^{6+} was from MoO_3 caused by the oxidation of MoS_2. The peak at 226.5 eV was indexed to S^{2-} of S 2s, which is in good agreement with the previous XPS studies.[36]

Figures 2g and **S4a-d** show the magnitude and phase spectra for transmission (S21) of the proposed piezoelectric cantilever operated at the first to fourth modes and sixth-order mode before the MoS_2 deposition, respectively.[37] The peak to peak value of the magnitude spectrum is quite small and the signal-to-noise ratio (SNR) of the transmission spectra is low. **Figure 2h** shows resistance and reactance spectra of the piezoelectric cantilever operated at the sixth mode before the MoS_2 deposition. There is no obvious resonance peak with a low SNR. **Figure 2i** and **S5a-d** show the magnitude and phase spectra for transmission of the cantilever after MoS_2 deposition. The peak to peak value and SNR of the transmission spectra have been significantly increased and the insertion loss is apparently reduced. The resonant frequencies of the cantilever are also reduced after the MoS_2 deposition because of the mass loading effect. **Figure 2j** shows the reactance and resistance spectra after the MoS_2 deposition. There are strong resonance peaks after the deposition of MoS_2 onto the cantilever. **Figures S6a** and **S6b** show the impedance values of the piezoelectric cantilever operated at the sixth mode before and after the MoS_2 deposition. These values are reduced after the film deposition. These results demonstrate that MoS_2 film works well as the top electrode.

Sensing Performances for Humidity Detection. The sensing mechanism of the MoS_2-based sensor to humidity is related to the adsorption of the water molecules onto the surface defects in the form of Mo-O bonds, which results in a physically absorbed water layer.[38] On the other hand, water molecules permeate into MoS_2 interlayers and increase their layer spacing, which also plays a crucial role in the responses of humidity sensing.[39] The frequency shift of the proposed sensor was applied as the response to humidity. The resonant frequency of the piezoelectric cantilever can be calculated by,[40]

$$f_n = (v_n^2/2\pi L^2)\sqrt{D_p/m} \qquad (1)$$

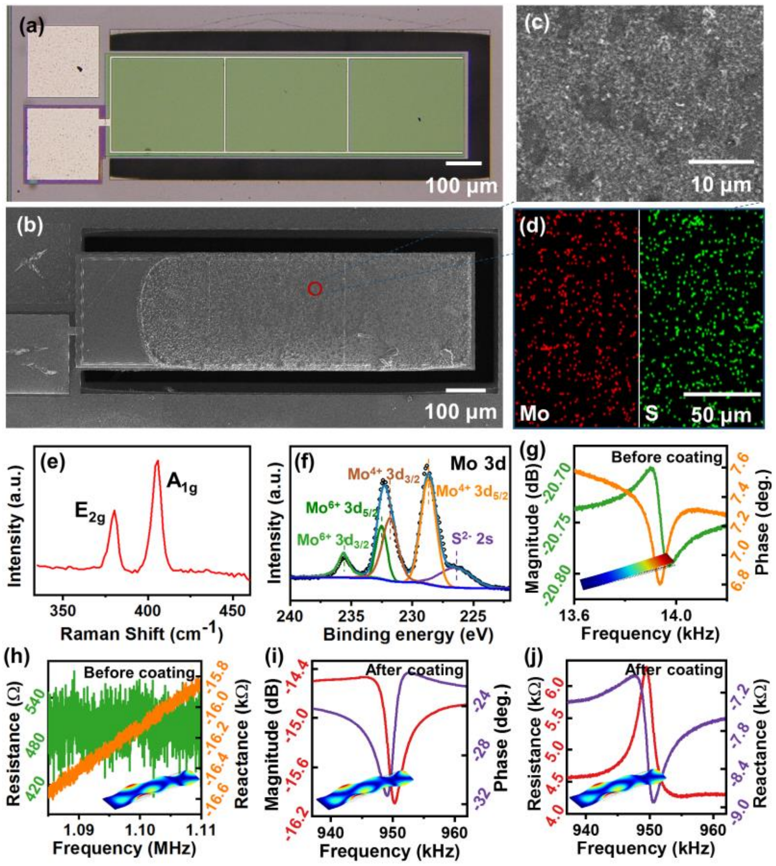

Figure 2. Characterizations of the fabricated environmental sensor. (a) An optical image of the piezoelectric cantilever. (b) An SEM image of the sensor after the MoS2 deposition. (c) Surface morphology of the MoS2 film. (d) EDS analysis for elements of Mo and S. (e) Raman spectrum of the MoS2 film. (f) XPS spectra for Mo 3d of the MoS2. Transmission spectra (g) and resistance and reactance spectra (h) of the cantilever before the MoS2 deposition. Transmission spectra (i) and resistance and reactance spectra (j) of the fabricated sensor.

where v_n, L, D_p, and m are the dimensionless eigenvalue, length, bending modulus per unit width, and mass per unit area of the sensor based on piezoelectric cantilever, respectively. After the adsorption of water molecules on the surface and into the interlayers of the MoS_2 film, the mass (m) increases, causing the frequency shifts of the sensor. Mass sensitivity of the sensor based on piezoelectric cantilever can be calculated by,[41]

$$\Delta f/\Delta M = (-v_n^2/8\sqrt{3}\pi L^3\omega\rho)\sqrt{E/\rho} \qquad (2)$$

where E, w, ρ, f, and M are the Young's modulus, width, density, resonant frequency, and mass of the sensor, respectively. Higher-order modes are associated with larger values of v_n. In order for achieving a good sensitivity, the frequency shift of the sixth-order resonant mode was applied as the response of the proposed sensor to humidity.

Figures S7a-i show the magnitude and phase spectra for transmission of the proposed sensor in the humidity range from 10% to 90% RH with an increment of 10% RH. For better visualization, they are plotted into **Figures 3a** and **3b**. The frequency of the sensor decreases as the humidity increases due to the mass loading effect caused by the adsorption of water molecules. Meanwhile, the insertion loss is significantly reduced and the peak to peak value and shape of the magnitude spectra are changed, which will be discussed in the next section.

Figure 3c show the frequency responses of the sensor to various humidity levels. The sensitivity of the sensor to humidity can be defined as,

$$S = |\Delta f|/\Delta RH \qquad (3)$$

where Δf and ΔRH are the frequency shift and humidity change, respectively. The sensitivity of the sensor at relatively low humidity (10-50%RH) is 130.59 Hz/%RH, whereas the sensitivity at relatively high humidity (60-90%RH) is 440.83 Hz/%RH. In low-humidity environments, the water molecules are absorbed by the MoS_2 film, resulting in the first physically absorbed water layer. With the increase of humidity, water molecules are absorbed not only by the MoS_2 film but also by the first water layer, resulting in an improved sensitivity.[39]

Figure 3d shows the frequency shifts of the sensor at very low (5%RH to 10%RH) and very high (90%RH to 95%RH) humidity conditions with an interval of 1%RH. The sensitivities of the sensor at low and high humidity conditions are ~159.86 Hz/%RH and ~550 Hz/%RH, respectively. In order to investigate the hysteresis performance of the proposed sensor, the humidity was changed from 10%RH to 90%RH and then returned to 10%RH. As shown in **Figure 3e**, a low hysteresis of the sensor was obtained (5.6%). The fluctuation in frequency shifts of the sensor was recorded at 30%RH and 80%RH, as shown in **Figure 3f**, indicating small fluctuations in frequency shifts. The resolution of the sensor was calculated by,

$$R = 3\sigma/S \qquad (4)$$

where σ and S are the standard deviations of the frequency shift and the sensitivity of the sensor at a given humidity. The obtained resolutions for the sensor at 30%RH and 80%RH are 0.78%RH and 0.30%RH, respectively.

The repeatability of the sensor was tested by changing the humidity between 0.1%RH and 90%RH over three cycles. The time interval between the two points was 0.2 s. **Figure 3g** shows the good short-term repeatability of the sensor. **Figures 3h** and **3i** show the detailed response and recovery processes of the sensor. The response and recovery times are defined as the time from when the resonant frequencies start to change until the frequency shifts reach 90% of their final value.[26] The response and recovery times of the sensor are 1 s and 2.8 s, respectively, which are much shorter than those of the literature-reported sensors as listed in **Table S1**, indicating the great potential of the proposed sensor for fast-response detection.

Detections of Temperature and CO_2 Concentration with the Interference of Humidity. **Figure S8** shows the equivalent circuit model of the piezoelectric cantilever-based sensor, where C_1, R_1, and L_1 are the "motional" components due to the electromechanical coupling. The C_1, R_1, and L_1 represent the mechanical elasticity of the sensor, the energy dissipation in vibration, and the mass of the sensor, respectively.[42] The C_0 and R_0 indicate the feedthrough capacitance between the top and bottom electrodes and dielectric loss in the thickness of MoS_2 and AlN film, respectively.[43] R_s stands for the sum of the resistances of the MoS_2 film and the contact resistance between the MoS_2 film and the metal leads, which does not exist in the equivalent circuit model of conventional piezoelectric cantilevers. The resistance of the model can be written as,

$$R = \left\{\gamma + \frac{[2\alpha\gamma - \beta^2\gamma^2(1+\gamma)](f/f_{LC})^2 + (1+\gamma)\alpha^2 - 2\alpha\gamma(1+\alpha)}{\sqrt{(f/f_{LC})^4 + [\beta^2(1+\gamma)^2 - 2(1+\alpha)](f/f_{LC})^2 + (1+\alpha)^2}}\right\} R_1 + R_s \qquad (5)$$

in which,

$$\alpha = C_1/C_0 \qquad (6)$$

$$\beta = R_1 C_1/\sqrt{L_1 C_1} \qquad (7)$$

$$\gamma = R_0/R_1 \qquad (8)$$

$$f_{LC} = 1/(2\pi\sqrt{L_1 C_1}) \qquad (9)$$

where f is the frequency of the resistance. The resistance data of the sensor from 935 kHz to 955 kHz were fitted using the equivalent model with a least square method. **Figure S9** shows that the fitting results using the equivalent model are quite close to the resistance spectrum of the piezoelectric cantilever-based sensor, indicating the high accuracy of the equivalent circuit model.

Each component in the equivalent circuit model has a unique effect on the transmission magnitude spectrum of the proposed sensor. For example, L_1 only affects the resonant frequency but not the insertion loss, while R_s only affects the insertion loss but not the resonant frequency. Therefore, the transmission magnitude spectrum reflects multiple properties of the sensor, such as mass, mechanical elasticity,

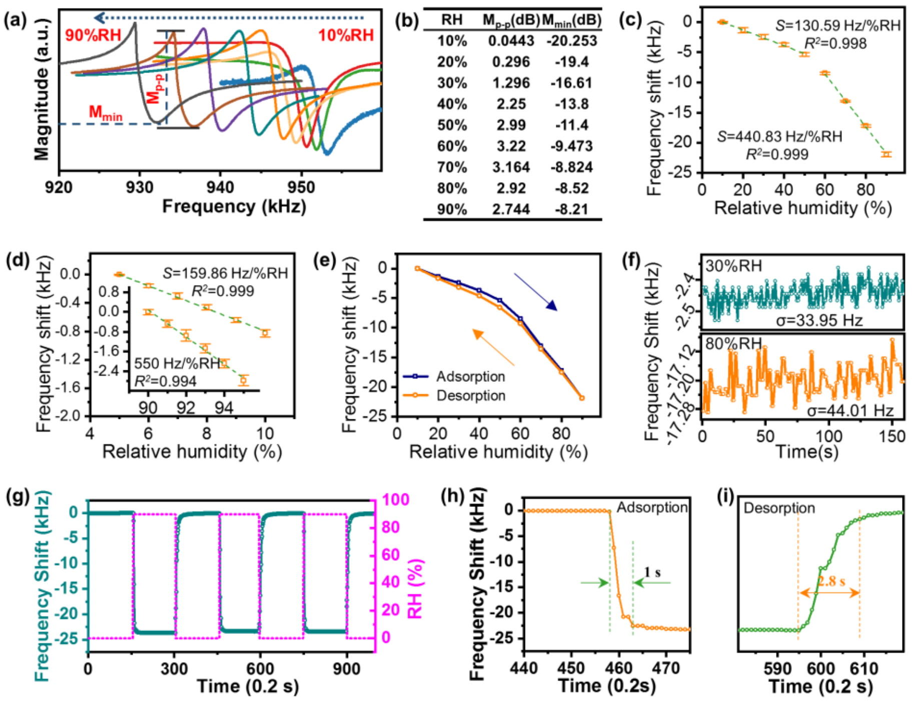

RH	$M_{p\text{-}p}$(dB)	M_{min}(dB)
10%	0.0443	-20.253
20%	0.296	-19.4
30%	1.296	-16.61
40%	2.25	-13.8
50%	2.99	-11.4
60%	3.22	-9.473
70%	3.164	-8.824
80%	2.92	-8.52
90%	2.744	-8.21

Figure 3. Sensing performances of the sensor for humidity detection. (a), (b) Magnitude spectra for the transmission of the sensor at various humidity levels. (c) Frequency shifts of the sensor from 10% to 90% RH. (d) Frequency shifts of the sensor at very low and high humidity. (e) The hysteresis performance of the sensor. (f) The fluctuations in frequency shifts at 30%RH and 80%RH. (g) Dynamic response of the sensor to humidity. Detailed response (h) and recovery (i) processes of the sensor.

and insertion loss, which are associated with different properties of the MoS_2 film.

The CO_2 and water molecules are absorbed on the defects and also inserted into interlayers of the MoS_2 film, thus changing the mass, viscosity, elasticity, and electrical conductivity of the sensing film, which are associated with the multiple components in the equivalent circuit model. Accordingly, adsorptions of water and CO_2 molecules cause the changes in position and shape of the magnitude spectrum for transmission of the proposed sensor. The change proportions of multiple components in the equivalent model caused by CO_2 and water molecules are quite different,[44, 45] and thus changes of the magnitude spectra for transmission are also different. Most conventional environmental sensors only detect changes in one single property of the sensing film (e.g., electrical conductivity), thus causing serious waste of much crucial information. The transmission magnitude spectra of the proposed sensor can be used to monitor the CO_2 and humidity simultaneously, thus making full use of the changes in multiple properties of MoS_2.

Figures S10a-i show the transmission magnitude spectra of the proposed sensor (at 50%RH) with the CO_2 concentration from 0% to 8%VOL and a step increment of 1%VOL. For better visualization, the data are plotted into **Figures 4a and 4b**. The frequency of the sensor decreases as the CO_2 concentration is increased, mainly due to the mass loading effect caused by the adsorption of CO_2. Meantime, the insertion loss is significantly reduced because of the improvement of electrical conductivity of the MoS_2 film.[38] The peak to peak values of the magnitude spectra are decreased because of the increase in energy dissipation caused by the changes in viscosity of the MoS_2 film and dielectric loss.[46, 47] **Figures S11a-i to Figures S13a-i** show the magnitude spectra for transmission of the sensor with the changes of CO_2 concentration at 30%RH, 40%RH, and 70%RH, respectively. **Figure 4c** shows the shifts in frequency and minimum magnitude value of the sensor vs. the changes of CO_2 concentration. Obviously, both of these two parameters can be used to monitor CO_2 concentration.

In order to fully use the signal outputs from the piezoelectric cantilever-based sensor, the magnitude spectra for transmission were used to monitor CO_2 concentration with the interference of humidity. As shown in **Figure 4d**, the magnitude spectrum was firstly discretized. In order to restore the shape and position of the spectra with the least amount of data, the minimum magnitude value in the spectrum (M_o) and its corresponding frequency (f_o) were firstly found. Because the difference between the corresponding frequencies of maximum and minimum magnitude values is always less than 4.5 kHz, we take a frequency every 500 Hz on the left side of f_o, a total of ten, and find their corresponding magnitudes (M_{-10}, M_{-9}, …, M_{-1}). Similarly, (M_{+1}, …, M_{+10}) were found on the right side of f_o. Then the resulting 22 characteristic parameters (M_{-10}, …, M_{+10}, and f_o) were input to an artificial neural network (ANN) model to obtain CO_2 concentrations with the interference of humidity. As shown in Figure 4d, the adopted ANN model is composed of eight layers with 50 neurons in each layer, which are input layer, linear layer, activation function, ..., and output layer, respectively.

Figure 4e shows the predicted CO_2 concentrations based on the obtained magnitude spectra at different humidity levels using the ANN model after 150 learning epochs, compared with the actual CO_2 concentration. All the points are close to the diagonal positions, indicating the high accuracy of the predictions. The prediction error (e) was defined as the differences between the predicted and actual concentrations and accuracy (p) was defined as,

$$p = 1 - |e|/c \qquad (10)$$

in which c is the actual concentration. **Figure S14a** shows the prediction accuracy and error for each point, revealing the average accuracy of 96.2%. Considering the small amount of data, the leave-one-out cross validation (LOOCV) was applied to evaluate the performance of the ANN model. **Figure 4f** shows the results of the LOOCV for the concentration prediction and **Figure S14b** shows the corresponding accuracy and error for each point, indicating a validation accuracy of 91.9%. In order to eliminate the error caused by the small data amount in the dataset, the dataset was amplified 5 times from 36 (i.e., 9 CO_2 concentrations × 4 humidity) to 180 data points by the synthetic minority oversampling technique (SMOTE) method. The amplified dataset was randomly divided into a test set and a training set, containing 45 and 135 data, respectively. The prediction accuracy of the ANN model for the test set is 93.3% after 150 learning epochs using the training dataset, revealing that CO_2 concentration with the interferences can be accurately monitored using the proposed sensor.

Similar to the CO_2 concentration, changes of temperature lead to the multiple properties of MoS_2 films, such as electrical conductivity, viscosity, and elasticity.[46, 47] The developed sensor was then used to monitor the temperature with the interference of humidity. Since the

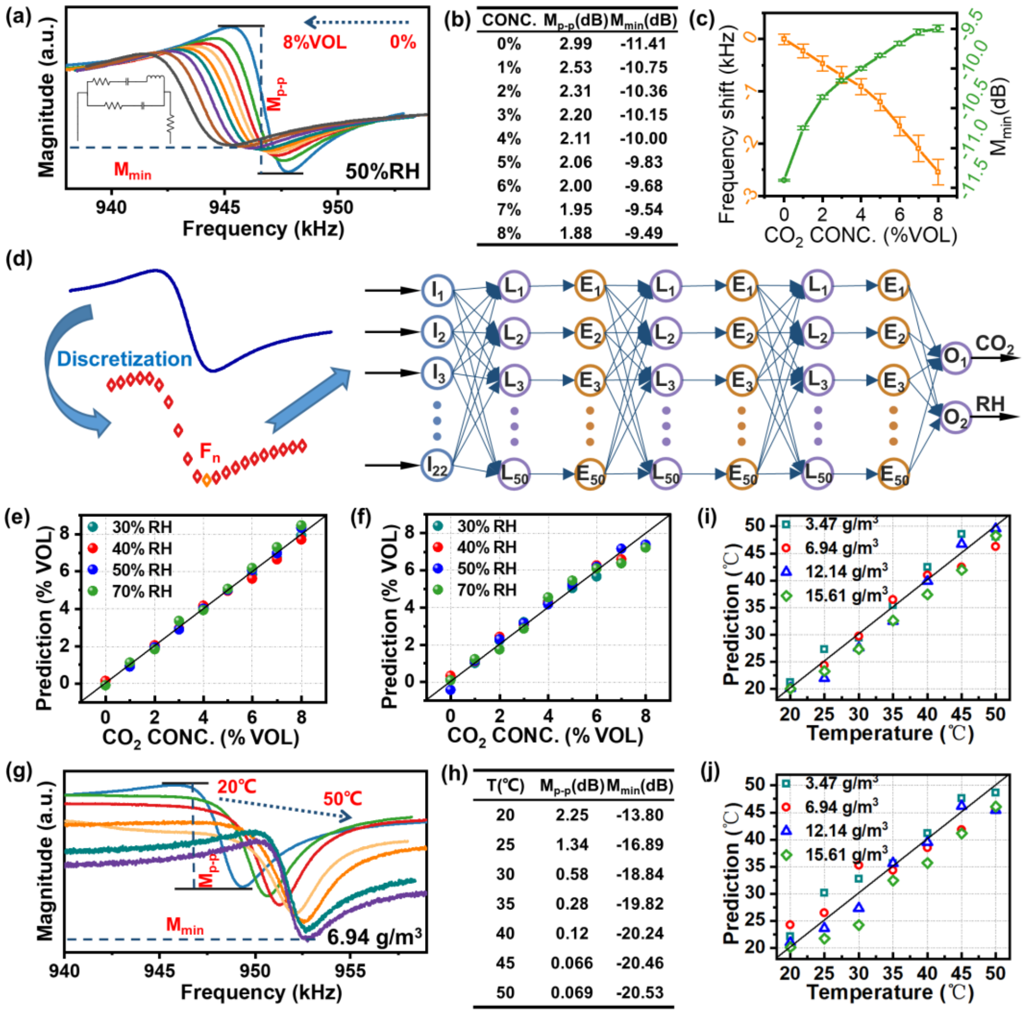

CONC.	M_{p-p}(dB)	M_{min}(dB)
0%	2.99	-11.41
1%	2.53	-10.75
2%	2.31	-10.36
3%	2.20	-10.15
4%	2.11	-10.00
5%	2.06	-9.83
6%	2.00	-9.68
7%	1.95	-9.54
8%	1.88	-9.49

T(℃)	M_{p-p}(dB)	M_{min}(dB)
20	2.25	-13.80
25	1.34	-16.89
30	0.58	-18.84
35	0.28	-19.82
40	0.12	-20.24
45	0.066	-20.46
50	0.069	-20.53

Figure 4. Detections of temperature and CO_2 concentration with the interference of humidity. (a), (b) Magnitude spectra for the transmission of the sensor at various CO_2 concentrations. (c) The shifts in frequency and minimum magnitude value of the sensor. (d) The scheme for CO_2 concentration prediction based on transmission magnitude spectra and the ANN model. (e) CO_2 concentration predictions in various humidity backgrounds. (f) LOOCV results for the CO_2 concentration predictions. (g), (h) Magnitude spectra for the transmission of the sensor at various temperatures. (i) Temperature predictions in various humidity backgrounds. (j) LOOCV results for the temperature prediction.

relative humidity varies with temperature, the magnitude spectra for transmission of the proposed sensor in the temperature range from 20°C to 50°C with a step increment of 5°C were obtained at different absolute humidity levels. **Figure S19a-g** shows the magnitude spectra at 6.94 g/cm^3 (absolute humidity). For better visualization, they are plotted into **Figures 4g** and **4h**. The relative humidity levels are gradually decreased as the temperature rises, resulting in increases of frequency and insertion loss and decreases of peak to peak value. **Figures S20a-g to Figures S22a-g** show the magnitude spectra for transmission of the sensor with the changes of temperature at 3.47 g/m^3, 12.14 g/m^3, and 15.61 g/m^3 (absolute humidity), respectively.

These magnitude spectra at different temperatures, and also those from 5%RH to 90%RH at a fixed temperature of 20°C were input into the ANN model. **Figure 4i** shows the predicted temperatures after 150 learning epochs vs. the actual temperatures at the different humidity conditions. All the points are close to the diagonal positions, indicating the high accuracy of the prediction. The prediction accuracy (p) was defined as,

$$p = 1 - |e|/T \qquad (11)$$

in which e and T are the prediction error and actual temperature (°C). **Figure S23a** shows the prediction accuracy and error for each point, revealing the average prediction accuracy of 95.3%. **Figure 4j** shows the result of the LOOCV for the temperature prediction, and **Figure S23b** shows the corresponding accuracy and error for each point, indicating the validation accuracy of 92.1%. The above results clearly show that temperature can be accurately detected in a background of variable humidity levels using the proposed sensor.

Real-Time Detections of Humidity and Temperature for Non-Contact Sensing. Based on the proposed sensor, a system was built to detect temperature and humidity in real time for non-contact sensing, as shown in **Figure 5a**. The magnitude spectrum of the sensor was discretized and input into a trained ANN model to obtain real-time data of both temperature and humidity. Three datasets were used to train the ANN model. The first dataset is the magnitude spectra from 5%RH to 95%RH at 20°C. The second dataset is the transmission magnitude spectra of the sensor with the changes of temperature at different absolute humidity levels. Since the temperature coefficient of frequency (TCF) of the piezoelectric cantilever-based sensor is approximately -20 ppm/°C,[26] the relative humidity levels in the second dataset can be calculated by the frequency. The finger, banana, and frozen dumpling were placed close (1-5 mm) to the commercial sensor and the proposed sensor ten times. The obtained temperature and humidity and transmission magnitude spectra constitute the third dataset, as shown in **Figure S25-27**.

To demonstrate the sensor's capability to detect temperature and humidity simultaneously, real-time detections of non-contact sensing for finger, banana, and frozen dumpling were performed. Evaporation of water molecules from a person's skin increases the humidity surrounding it and gradient fields of both humidity and temperature are generated around the finger.[48] As shown in **Figure 5b**, the humidity level and temperature are increased when the finger is moved close to the proposed sensor. Whereas the humidity and temperature are recovered to their original values when the finger is moved away. By moving the finger closer and then away from the sensor cyclically, the proposed sensor exhibits its ability to continuously monitor environmental humidity and temperature. The monitoring process is detailed in **Video S1** (supporting information). **Figure 5c** shows a typical non-contact sensing process for finger, with the obtained humidity and temperature of 90%RH and 25.5°C, respectively.

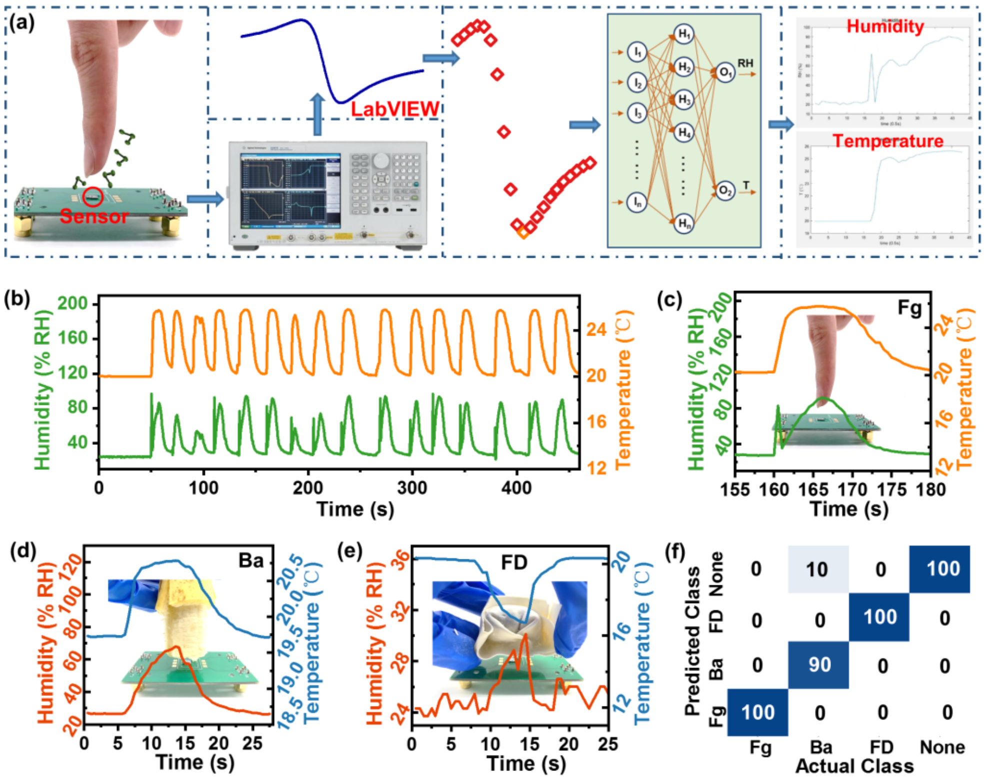

Figure 5. Real-time detections of humidity and temperature for non-contact sensing. (a) The system for real-time parameter detections in non-contact sensing. (b) Real-time humidity and temperature in non-contact sensing for finger. Typical processes of the non-contact sensing for (c) finger (Fg), (d) banana (Ba), and (e) frozen dumpling (FD). (f) The results of object recognition based on real-time humidity and temperature.

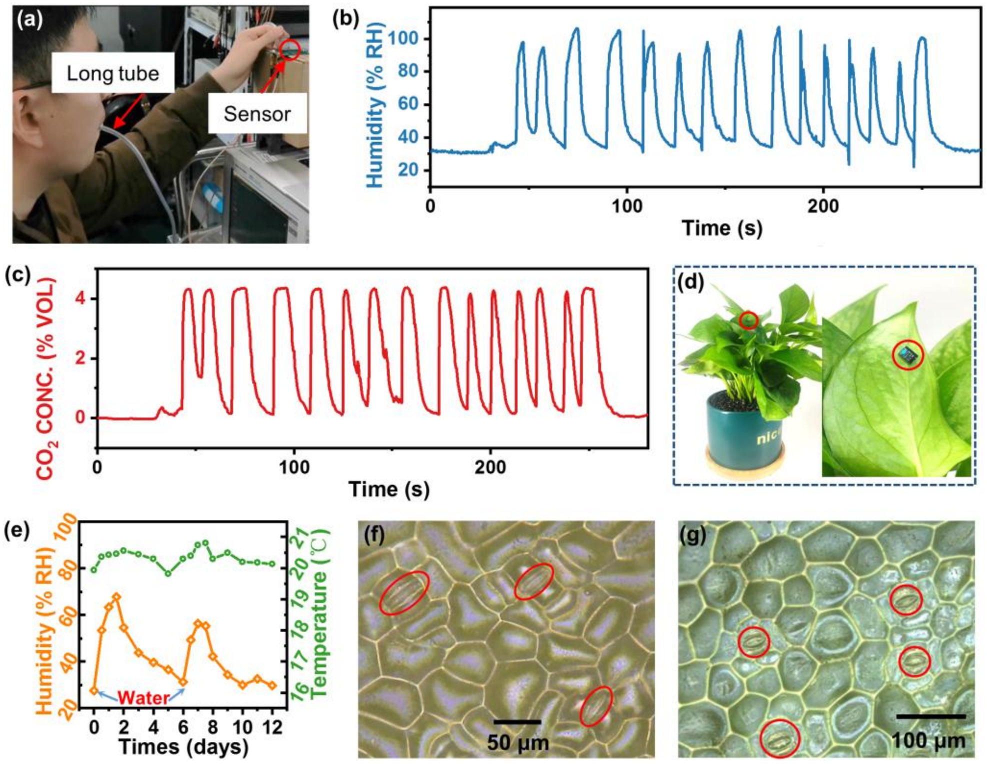

Figure 6. Detections of the parameters for monitoring human breath and plant ecosystem. (a) Photograph of the setup for human breath detection. Real-time humidity (b) and CO_2 concentration (c) in human breath. (d) Photograph of the sensor attached to the leaf surface. (e) The humidity and temperature in plant ecosystem for 12 days. Optical images of the plant leaf after watering for 6 days (f) and 1 day (g).

Figures 5d and **5e** show the typical processes of non-contact sensing for banana and frozen dumpling, respectively. The humidity was changed significantly and the temperature was changed slightly when the banana was moved close to the sensor. Whereas the temperature was apparently decreased when the frozen dumpling was moved near to the sensor. **Videos S2** and **S3** show the detailed monitoring processes for banana and frozen dumpling, respectively. Furthermore, the finger, banana, and frozen dumpling were placed close to the proposed sensor and the obtained humidity and temperature values were then input to a linear discriminant analysis (LDA) model for object recognition when the humidity is greater than 50%RH or the temperature is lower than 19°C. The details are shown in Videos S2&S3 (top right-hand corner). **Figure 5f** shows the recognition results for finger, banana, and frozen dumpling, indicating the high accuracy (97.5%) of the object recognition using the proposed sensor. "None" means the changes in humidity and temperature did not reach the threshold for object recognition. These results show that the proposed sensor has the potentials for non-contact sensing and human-machine interfacing.

Detections of Environmental Parameters for Monitoring Human Breath and Plant Ecosystem. The proposed sensor was then applied to detect real-time CO_2 concentration and humidity in human breath. As illustrated in **Figure 6a**, during the detection processes, human exhalation was blown to the proposed sensor through a long tube to cool down and avoid the influence of the significant influence from the temperature of exhalation. The transmission magnitude spectrum of the sensor was obtained and input into a trained ANN model to obtain real-time signals of CO_2 concentration and humidity. The ANN model was trained using three datasets. The first dataset was the magnitude spectra for transmission of the sensor from 5%RH to 95%RH at 20°C. The second dataset was the magnitude spectra for transmission of the sensor with the changes of CO_2 concentration at different relative humidity levels. The exhalation was blown to both a commercial sensor and the proposed sensor for ten times. The third dataset was the obtained CO_2 concentrations and humidity levels, as well as the transmission magnitude spectra, as shown in **Figure S28**.

Figures 6b and **6c** show the changes of humidity and CO_2 concentration in the processes of human deep breaths. The humidity and CO_2 concentration are increased rapidly in the exhalation process, which is due to the exhaled CO_2 and water vapor by a human. The humidity and CO_2 concentration are then returned to normal values in the inhalation process. The concentration of CO_2 in human exhalation is 4.3%Vol and the humidity level occasionally exceeds 100% due to temperature disturbances and calculation errors. The detailed sensing process is shown in **Video S4**. These results show that both the humidity and CO_2 concentration in the human breath process can be continuously monitored using the proposed sensor.

The proposed sensor was further applied for long-term monitoring of the humidity and temperature for a plant ecosystem, aiming to monitor the external environment which will significantly affect the growth of plants. As shown in **Figure 6d**, the proposed sensor was attached to the surface of the Epipremnum aureum to detect the humidity and temperature on the leaf surface. **Figure 6e** shows the variations in humidity and temperature on the leaf surface over 12 days. The humidity was significantly increased after watering the plants and then decrease with the increase of past time, indicating the water conditions of the plant affect the humidity levels on the surface of plants. **Figure 6f** shows an optical image of the plant leaf after watering for 6 days, in which the stomata were closed to prevent water loss. **Figure 6g** shows an optical image of the leaf after watering for 1 day, in which the stomata are opened to release water molecules from the leaves, increasing humidity on the plant surface.

CONCLUSIONS

In conclusion, a multifunctional environmental sensor was proposed based on one single sensing element. A MoS_2 film was deposited on the surface of the cantilever and used as both the sensing layer and top electrode, forming the environmental sensor. The proposed sensor shows good performances for humidity detection, such as high resolution (0.3%RH), low hysteresis (5.6%), and fast response (1 s) and recovery (2.8 s). Based on the machine learning algorithms, the temperature and CO_2 with the interference of humidity can be quantified using the proposed sensor with the accuracies of 91.9% and 92.1%, respectively. Furthermore, the sensor was successfully applied in real-time detections of humidity and temperature or CO_2 concertation for non-contact sensation and monitoring human breath and plant ecosystem. These results indicate the great potentials of the proposed sensor in human-machine interaction and health monitoring of plants and human beings. The scheme of this work could be easily adapted to other multifunctional sensors.

EXPERIMENTAL SECTION

Design, Fabrication, and Characterization of the Proposed Sensor. **Figure S29** shows the schematic illustration of the proposed sensor, which is composed of a sensing layer of MoS_2 and piezoelectric cantilever based on AlN film. The piezoelectric cantilever consists of an AlN layer of 0.5 μm and a Si layer of 10 μm. The thickness of the insulating layer between the top and bottom electrodes is 0.2 μm. The fabrication process of the cantilever began with a highly N-doped SOI wafer, as shown in **Figure S30**. Then the thermal oxide layer, AlN layer, and metal leads were deposited and patterned in sequence. Finally, the device and handle layers of SOI were patterned and micromachined into a cantilever structure successively. Then MoS_2 dispersion with a concentration of 0.15 mg ml^{-1} was deposited onto the surface of the cantilever and dried in a vacuum chamber. The MoS_2 dispersion was purchased from Nanjing Xianfeng nanomaterial technology Co., Ltd.

An SEM (SU-3500, Hitachi) with an EDS (X-max20, Oxford) was used to observe the surface morphology and obtain the element distributions of the MoS_2 film. Raman spectroscopy analysis was performed using a commercial Raman spectrometer (LabRAM HR evolution, HORIBA JOBIN YVON). Chemical components and bonding structures of the sensing film were studied using an XPS (Escalab 250Xi, Thermo Fisher). Gaussian–Lorentzian method was adopted to conduct the curve fitting and calculations for the XPS results.

Experimental Setup. A schematic illustration of the experimental setup for environmental sensing is shown in Figure **S31**. The sensor was fixed in a metallic chamber of 86 cm^3. The gas sources were split into two components, one of which was flowed through the DI water, and then they were mixed in the chamber. The humidity in this chamber can be manipulated by adjusting the flow rates of the two flows. The CO_2 concentration in this chamber was manipulated by adjusting the mass flows of dry air and CO_2 separately. The parameters in the chamber were calibrated by a commercial hygrometer (TASI-621) and CO_2 sensor (MH-Z16). The transmission spectra of the sensor were recorded using a network analyzer (Agilent E5061B) with a LabView program. All the experiments were carried out at room temperature (20 ± 0.5°C).

Data Analysis Methods. The measurements were made in triplicate, and results were expressed as the mean of the results ± their standard deviation. The transmission spectra of the sensor were obtained by a LabVIEW program. The discretization of the spectra and machine learning algorithms were carried out using the program in Matlab. The 22 characteristic parameters from the transmission spectra were input to the ANN model to obtain real-time humidity and temperature or CO_2 concentration. The LDA was performed as a supervised pattern recognition tool for object recognition. Due to the small amount of data, the LOOCV and hold-out methods were both applied as the validation methods to evaluate the performance of the models. The SMOTE was adopted to amplify the datasets. Details of the validation methods and SMOTE were shown in Supporting Information.

ASSOCIATED CONTENT

Supporting Information. Comparison for response/recovery times of the humidity sensors; schematic illustrations of the conventional piezoelectric cantilever-based environmental sensor, the proposed multifunctional sensor, and the experimental setup; optical images of the fabricated cantilever; equivalent circuit model for the proposed sensor; supplementary experimental results. (PDF)

Humidity and temperature monitoring in non-contact sensing for finger. (Video)

Non-contact sensing and object recognition processes for banana. (Video)

Non-contact sensing and object recognition processes for frozen dumpling. (Video)

Humidity and CO_2 concentration detections in human breath. (Video)

NOTES

The authors declare no competing financial interest.

ACKNOWLEDGMENT

This work is supported by the "Zhejiang Provincial Natural Science Foundation of China (LZ19E050002)", and the "National Natural Science Foundation of China (NSFC 51875521, 52175552)". the UK Engineering and Physical Sciences Research Council (EPSRC) under grant EP/P018998/1, International Exchange Grant (IEC/NSFC/201078) through Royal Society UK and the NSFC.

REFERENCES

1. Kim, I.; Kim, W.-S.; Kim, K.; Ansari, M. A.; Mehmood, M. Q.; Badloe, T.; Kim, Y.; Gwak, J.; Lee, H.; Kim, Y.-K.; Rho, J., Holographic Metasurface Gas Sensors for Instantaneous Visual Alarms. *Sci. Adv.* **2021,** *7,* eabe9943.

2. Li, D.; Shao, Y.; Zhang, Q.; Qu, M.; Ping, J.; Fu, Y.; Xie, J., A Flexible Virtual Sensor Array Based on Laser-Induced Graphene and Mxene for Detecting Volatile Organic Compounds in Human Breath. *Analyst* **2021,** *146,* 5704-5713.

3. Hu, H.; Yang, X.; Guo, X.; Khaliji, K.; Biswas, S. R.; García de Abajo, F. J.; Low, T.; Sun, Z.; Dai, Q., Gas Identification with Graphene Plasmons. *Nat. Commun.* **2019,** *10,* 1131.

4. Li, Z.; Paul, R.; Ba Tis, T.; Saville, A. C.; Hansel, J. C.; Yu, T.; Ristaino, J. B.; Wei, Q., Non-Invasive Plant Disease Diagnostics Enabled by Smartphone-Based Fingerprinting of Leaf Volatiles. *Nat. Plants* **2019,** *5,* 856-866.

5. Chan, L. W.; Anahtar, M. N.; Ong, T.-H.; Hern, K. E.; Kunz, R. R.; Bhatia, S. N., Engineering Synthetic Breath Biomarkers for Respiratory Disease. *Nat. Nanotechnol.* **2020,** *15,* 792-800.

6. Kim, S.-J.; Choi, S.-J.; Jang, J.-S.; Kim, N.-H.; Hakim, M.; Tuller, H. L.; Kim, I.-D., Mesoporous Wo3 Nanofibers with Protein-Templated Nanoscale Catalysts for Detection of Trace Biomarkers in Exhaled Breath. *ACS Nano* **2016,** *10,* 5891-5899.

7. Lu, Y.; Xu, K.; Zhang, L.; Deguchi, M.; Shishido, H.; Arie, T.; Pan, R.; Hayashi, A.; Shen, L.; Akita, S.; Takei, K., Multimodal Plant Healthcare Flexible Sensor System. *ACS Nano* **2020,** *14,* 10966-10975.

8. Majumder, B. D.; Roy, J. K.; Padhee, S., Recent Advances in Multifunctional Sensing Technology on a Perspective of Multi-Sensor System: A Review. *IEEE Sens. J.* **2019,** *19,* 1204-1214.

9. Luo, C.; Jia, J.; Gong, Y.; Wang, Z.; Fu, Q.; Pan, C., Highly Sensitive, Durable, and Multifunctional Sensor Inspired by a Spider. *ACS Appl. Mater. Interfaces* **2017,** *9,* 19955-19962.

10. Wang, B.; Thukral, A.; Xie, Z.; Liu, L.; Zhang, X.; Huang, W.; Yu, X.; Yu, C.; Marks, T. J.; Facchetti, A., Flexible and Stretchable Metal Oxide Nanofiber Networks for Multimodal and Monolithically Integrated Wearable Electronics. *Nat. Commun.* **2020,** *11,* 2405.

11. Kim, T.; Lee, S.; Hong, T.; Shin, G.; Kim, T.; Park, Y.-L., Heterogeneous Sensing in a Multifunctional Soft Sensor for Human-Robot Interfaces. *Sci. Rob.* **2020,** *5,* eabc6878.

12. Gui, Q.; He, Y.; Gao, N.; Tao, X.; Wang, Y., A Skin - Inspired Integrated Sensor for Synchronous Monitoring of Multiparameter Signals. *Adv. Funct. Mater.* **2017,** *27,* 1702050.

13. Xu, K.; Fujita, Y.; Lu, Y.; Honda, S.; Shiomi, M.; Arie, T.; Akita, S.; Takei, K., A Wearable Body Condition Sensor System with Wireless Feedback Alarm Functions. *Adv. Mater.* **2021,** *33,* 2008701.

14. Xu, H.; Xiang, J. X.; Lu, Y. F.; Zhang, M. K.; Li, J. J.; Gao, B. B.; Zhao, Y. J.; Gu, Z. Z., Multifunctional Wearable Sensing Devices Based on Functionalized Graphene Films for Simultaneous Monitoring of Physiological Signals and Volatile Organic Compound Biomarkers. *ACS Appl. Mater. Interfaces* **2018,** *10,* 11785-11793.

15. Bokka, N.; Selamneni, V.; Sahatiya, P. A water destructible SnS_2QD/PVA film based transient multifunctional sensor and machine learning assisted stimulus identification for non-invasive personal care diagnostics. *Mat. Adv.* **2020,** *1,* 2818-2830.

16. Hajizadegan, M.; Sakhdari, M.; Abbasi, S.; Chen, P.-Y. Machine Learning Assisted Multi-Functional Graphene-Based Harmonic Sensors. *IEEE Sens. J.* **2021,** *21,* 8333-8340.

17. Wei, C.; Lin, W.; Liang, S.; Chen, M.; Zheng, Y.; Liao, X.; Chen, Z. An All-In-One Multifunctional Touch Sensor with Carbon-Based Gradient Resistance Elements. *Nano-micro Lett.* **2022,** *14,* 131.

18. Le, X.; Shi, Q.; Vachon, P.; Ng, E. J.; Lee, C. Piezoelectric MEMS—evolution from sensing technology to diversified applications in the 5G/Internet of Things (IoT) era. *J. Micromech. Microeng.* **2022,** *32,* 014005.

19. Zhu, J.; Liu, X.; Shi, Q.; He, T.; Sun, Z.; Guo, X.; Liu, W.; Sulaiman, O. B.; Dong, B.; Lee, C. Development Trends and Perspectives of Future Sensors and MEMS/NEMS. *Micromach.* **2020,** *11,* 7.

20. Ren, Z.; Xu, J.; Le, X.; Lee, C. Heterogeneous Wafer Bonding Technology and Thin-Film Transfer Technology-Enabling Platform for the Next Generation Applications beyond 5G. *Micromach.* **2021,** *12,* 946.

21. Clément, P.; Del Castillo Perez, E.; Gonzalez, O.; Calavia, R.; Lucat, C.; Llobet, E.; Debéda, H., Gas Discrimination Using Screen-Printed Piezoelectric Cantilevers Coated with Carbon Nanotubes. *Sens. Actuators, B* **2016,** *237,* 1056-1065.

22. Sharma, H.; Mutharasan, R., Rapid and Sensitive Immunodetection of Listeria Monocytogenes in Milk Using a Novel Piezoelectric Cantilever Sensor. *Biosens. Bioelectron.* **2013,** *45,* 158-162.

23. Zhou, L.; Kato, F.; Nakamura, N.; Oshikane, Y.; Nagakubo, A.; Ogi, H., MEMS Hydrogen Gas Sensor with Wireless Quartz Crystal Resonator. *Sens. Actuators, B* **2021,** *334,* 129651.

24. Penza, M.; Aversa, P.; Cassano, G.; Suriano, D.; Wlodarski, W.; Benetti, M.; Cannata, D.; Pietrantonio, F. D.; Verona, E., Thin-Film Bulk-Acoustic-Resonator Gas Sensor Functionalized with a Nanocomposite Langmuir–Blodgett Layer of Carbon Nanotubes. *IEEE Trans. Electron Devices* **2008,** *55,* 1237-1243.

25. Zhang, L.; Yang, H.; Tan, Q.; Jing, L.; Zhang, W.; Xiong, J.; Chen, P.-Y., Wireless Detection of Biogenic Amines Using a Split-Ring Resonator with Silver Nanoparticles-Decorated Molybdenum Disulfide. *Sens. Actuators, B* **2021,** *343,* 130155.

26. Li, D.; Zhu, B.; Pang, K.; Zhang, Q.; Qu, M.; Liu, W.; Fu, Y.; Xie, J., Virtual Sensor Array Based on Piezoelectric Cantilever Resonator for Identification of Volatile Organic Compounds. *ACS Sens.* **2022,** 7, 1555-1563.

27. Bao, Y.; Xu, P.; Cai, S.; Yu, H.; Li, X., Detection of Volatile-Organic-Compounds (VOCs) in Solution Using Cantilever-Based Gas Sensors. *Talanta* **2018,** *182,* 148-155.

28. Li, D.; Liu, G.; Zhang, Q.; Qu, M.; Fu, Y. Q.; Liu, Q.; Xie, J., Virtual Sensor Array Based on MXene for Selective Detections of VOCs. *Sens. Actuators, B* **2021,** *331,* 129414.

29. Jiang, G.; Goledzinowski, M.; Comeau, F. J. E.; Zarrin, H.; Lui, G.; Lenos, J.; Veileux, A.; Liu, G.; Zhang, J.; Hemmati, S.; Qiao, J.; Chen, Z., Free-Standing Functionalized Graphene Oxide Solid Electrolytes in Electrochemical Gas Sensors. *Adv. Funct. Mater.* **2016,** *26,* 1729-1736.

30. Li, D.; Le, X.; Pang, J.; Peng, L.; Xu, Z.; Gao, C.; Xie, J., A Saw Hydrogen Sensor Based on Decoration of Graphene Oxide by Palladium Nanoparticles on Ain/Si Layered Structure. *J. Micromech. Microeng.* **2019,** *29,* 045007.

31. Wu, F.; Tian, H.; Shen, Y.; Hou, Z.; Ren, J.; Gou, G.; Sun, Y.; Yang, Y.; Ren, T.-L., Vertical Mos2 Transistors with Sub-1-nm Gate Lengths. *Nat.* **2022,** *603,* 259-264.

32. Pham, T.; Li, G.; Bekyarova, E.; Itkis, M. E.; Mulchandani, A., MoS_2-Based Optoelectronic Gas Sensor with Sub-Parts-Per-Billion Limit of NO_2 Gas Detection. *ACS Nano* **2019,** *13,* 3196-3205.

33. Zhou, Y.; Gao, C.; Guo, Y., Uv Assisted Ultrasensitive Trace No 2 Gas Sensing Based on Few-Layer MoS_2 Nanosheet–ZnO Nanowire Heterojunctions at Room Temperature. *J. Mater. Chem. A* **2018,** *6,* 10286-10296.

34. Zhao, J.; Li, N.; Yu, H.; Wei, Z.; Liao, M.; Chen, P.; Wang, S.; Shi, D.; Sun, Q.; Zhang, G., Highly Sensitive MoS_2 Humidity Sensors Array for Noncontact Sensation. *Adv. Mater.* **2017,** *29,* 1702076.

35. Zhang, D.; Jiang, C.; Wu, J., Layer-by-Layer Assembled In_2O_3 Nanocubes/Flower-Like Mos2 Nanofilm for Room Temperature Formaldehyde Sensing. *Sens. Actuators, B* **2018,** *273,* 176-184.

36. Zhao, P.; Tang, Y.; Mao, J.; Chen, Y.; Song, H.; Wang, J.; Song, Y.; Liang, Y.; Zhang, X., One-Dimensional MoS_2-Decorated TiO_2 Nanotube Gas Sensors for Efficient Alcohol Sensing. *J. Alloys Compd.* **2016,** *674,* 252-258.

37. Lee, J. E. Y.; Seshia, A. A., Direct Parameter Extraction in Feedthrough-Embedded Capacitive Mems Resonators. *Sens. Actuators, A* **2011,** *167,* 237-244.

38. Zhang, D.; Sun, Y. e.; Li, P.; Zhang, Y., Facile Fabrication of MoS_2-Modified SnO_2 Hybrid Nanocomposite for Ultrasensitive Humidity Sensing. *ACS Appl. Mater. Interfaces* **2016,** *8,* 14142-14149.

39. Li, X.; Tan, Q.; Qin, L.; Zhang, L.; Liang, X.; Yan, X., A High-Sensitivity MoS_2/Graphene Oxide Nanocomposite Humidity Sensor Based on Surface Acoustic Wave. *Sens. Actuators, A* **2022,** *341,* 113573.

40. Yi, J. W.; Shih, W. Y.; Shih, W.-H., Effect of Length, Width, and Mode on the Mass Detection Sensitivity of Piezoelectric Unimorph Cantilevers. *J. Appl. Phys.* **2002,** *91,* 1680-1686.

41. Li, D.; Dong, H.; Xie, Z.; Zhang, Q.; Qu, M.; Fu, Y.; Xie, J., High Resolution and Fast Response of Humidity Sensor Based on AlN Cantilever with Two Groups of Segmented Electrodes. *IEEE Electron Device Lett.* **2021,** *42,* 923-926.

42. Zhang, D.; Chen, H.; Zhou, X.; Wang, D.; Jin, Y.; Yu, S., In-Situ Polymerization of Metal Organic Frameworks-Derived $ZnCo_2O_4$/Polypyrrole Nanofilm on QCM Electrodes for Ultra-Highly Sensitive Humidity Sensing Application. *Sens. Actuators, A* **2019,** *295,* 687-695.

43. Li, D.; Xie, Z.; Qu, M.; Zhang, Q.; Fu, Y.; Xie, J., Virtual Sensor Array Based on Butterworth–Van Dyke Equivalent Model of QCM for Selective Detection of Volatile Organic Compounds. *ACS Appl. Mater. Interfaces* **2021,** *13,* 47043-47051.

44. Gao, F.; Boussaid, F.; Xuan, W.; Tsui, C.; Bermak, A., Dual Transduction Surface Acoustic Wave Gas Sensor for VOC Discrimination. *IEEE Electron Device Lett.* **2018,** *39,* 1920-1923.

45. Gao, F.; Xuan, W.; Bermak, A.; Boussaid, F.; Tsui, C.-Y.; Luo, J., Dual Transduction on a Single Sensor for Gas Identification. *Sens. Actuators, B* **2019,** *278,* 21-27.

46. Hamilton, M. A.; Alvarez, L. A.; Mauntler, N. A.; Argibay, N.; Colbert, R.; Burris, D. L.; Muratore, C.; Voevodin, A. A.; Perry, S. S.; Sawyer, W. G., A Possible Link between Macroscopic Wear and Temperature Dependent Friction Behaviors of MoS_2 Coatings. *Tribol. Lett.* **2008,** *32,* 91-98.

47. Wei, Y.; Hu, C.; Muhammad, Y.; Chen, L.; Zhou, D.; Wang, S.; Li, J.; Chen, Q., Fabrication and Performance Evaluation of Aminopropyl Triethoxysilane-

Dopamine-MoS_2 Incorporated SbS Modified Asphalt. *Constr. Build. Mater.* **2020,** *265,* 120346.

48. Dong, H.; Li, D.; Pang, J.; Zhang, Q.; Xie, J. In *Highly Sensitive and Fast-Response Humidity Sensor Based on SAW Resonator and MoS_2 for Human Activity Detection*, 2021 IEEE 34th *Int. Conf. Micro Electro Mech. Syst. (MEMS)*, IEEE: 2021; pp 322-325.

TOC

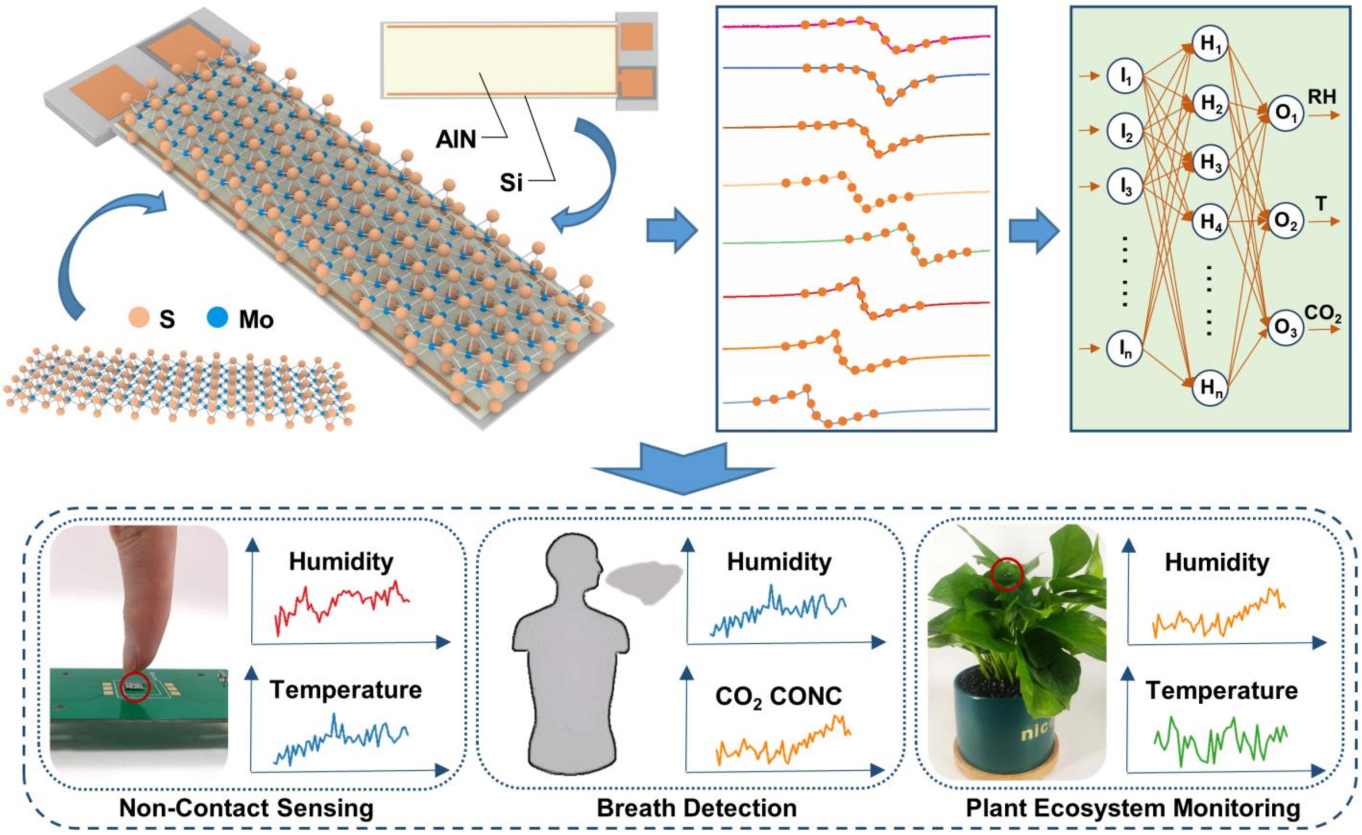
AlN
Si
S
Mo
I_1
I_2
I_3
I_n
H_1
H_2
H_3
H_4
H_n
O_1
O_2
O_3
RH
T
CO_2
Humidity
Temperature
Humidity
CO_2 CONC
Humidity
Temperature
Non-Contact Sensing
Breath Detection
Plant Ecosystem Monitoring